inorganics

MDPI

Article

Ultralight Cellulose-Derived Carbon Nanofibers from Freeze-Drying Emulsion Towards Superior Microwave Absorption

Anran Li [1,2], Zongquan Li [1,*] and Lei Qian [2,*]

[1] Key Laboratory of Pulp and Paper Science & Technology of Ministry of Education, Qilu University of Technology (Shandong Academy of Sciences), Jinan 250353, China; anran113sdu@163.com
[2] School of Materials Science and Engineering, Shandong University, 17923 Jingshi Road, Jinan 250061, China
* Correspondence: lizongquan@qlu.edu.cn (Z.L.); qleric@sdu.edu.cn (L.Q.)

Abstract: Carbon nanofibers (CNFs) are usually prepared by the carbonization of cellulose aerogels obtained from freeze-drying. However, cellulose with low concentration (below 1 wt%) is required to maintain the good porosity of the aerogels due to the strong hydrogen bonding between the cellulose molecules. In order to address this problem, here, ultralight cellulose-derived CNFs have been fabricated by freeze-drying cyclohexane (CHE)/cellulose nanofiber emulsions and carbonization. Field emission scanning electron microscopy, Raman spectroscopy, X-ray diffraction, X-ray photoelectron spectroscopy, and Fourier transform infrared spectroscopy are used to characterize the resulting CNFs. It is found that the CNFs consist of three-dimensional carbon networks, whose microstructure is easily adjusted by changing the CHE ratio (from 0 to 25 vol%) in the emulsions. The CNFs with high porosity are attributed to the fact that CHE as the oil phase can effectively weaken the hydrogen bonding and reduce the aggregation of the cellulose nanofibers. Carbon lattice defects and residual oxygen-containing functional groups are regarded as polarization centers, leading to the enhancement of dielectric loss. The conductive carbon networks also improve the conductive loss. All these factors improve the microwave absorption performance of the CNFs. So, the produced CNFs exhibit a superior electromagnetic wave performance with a minimum reflection loss of −42.18 dB and effective absorption bandwidth up to 4.9 GHz at 2 mm with a filling ratio of 2 wt%. This work provides a simple, low-cost, and sustainable synthesis route for CNFs used for ultralight high-performance microwave absorption materials.

Keywords: carbon nanofiber; cellulose nanofiber; freeze-drying; microwave absorption

Citation: Li, A.; Li, Z.; Qian, L. Ultralight Cellulose-Derived Carbon Nanofibers from Freeze-Drying Emulsion Towards Superior Microwave Absorption. *Inorganics* **2024**, *12*, 272. https://doi.org/10.3390/inorganics12110272

Academic Editors: Ben McLean and Alister Page

Received: 26 September 2024
Revised: 15 October 2024
Accepted: 21 October 2024
Published: 23 October 2024

1. Introduction

With the development of modern science and technology, various electronic devices have provided high efficiency for social production and allow great convenience for humans. The widespread application of electromagnetic waves has created a new pollution source that affects normal communication and threatens human health [1–3]. In recent years, microwave absorption (MA) materials have attracted great attention and have a special position not only in the military but in the civilian field. MA materials can absorb the energy of electromagnetic waves and convert them into thermal energy or other forms of energy [4,5]; they are utilized to address electromagnetic wave pollution. However, MA materials still need to meet the requirements of "thin, light, wide and strong" in modern society, that is, a thin coating thickness, light weight, wide effective absorption band, and strong reflection loss capacity [5–7].

Carbon-based MA materials have gradually attracted people's attention owing to their low density, adjustable dielectric properties, good environmental stability, and excellent MA capabilities [8,9]. Recently, porous carbon, carbon nanotubes, reduced graphene oxide, graphene, and carbon nanofibers (CNFs) have been successfully applied to the field of

electromagnetic wave absorption due to their high electrical conductivity and special nanostructures [2,10–18]. However, the low yield and expensive cost of these carbon nanomaterials limit their practical applications, and the development and application of new carbon materials have remained challenges for carbon-based MA materials until now.

Biomass materials are inexhaustible, renewable, widely distributed, and abundant resources present around the world [19]. However, until now, many biomass resources have not been effectively utilized. Natural cellulose, the skeleton of plants, is the most common form of biomass and natural biopolymer stored in the Earth [19,20]. Similar to biopolymers [21,22], cellulose nanofibers have been used in various fields such as biology, energy, and electromagnetic shields [5,23,24]. Meanwhile, cellulose nanofibers are a good precursor for preparing CNFs because of their low-cost, superior hydrophilicity, and their ability to preserve the fiber structure after carbonization [25,26]. Ehsan et al. [27,28] firstly investigated the possibility of fabricating CNFs from freeze-dried cellulose nanofibers and the effects of pyrolysis conditions. It was found that the heat treatment played an important role in the morphologies of the resulting CNFs. Zhao et al. [29] reported a carbon aerogel containing graphene, polyvinyl alcohol, and cellulose nanofibers with a high porosity and adsorption capacity, good compressibility, and perfect recyclability. Chen et al. [30] fabricated asymmetric supercapacitors based on bacterial-cellulose-derived CNFs@MnO_2 and nitrogen-doped CNFs, which retained excellent cycling stability with 95.4% of the initial capacity after 2000 cycles. And some studies have also declared that the three-dimensional conductive networks of CNFs could generate more effective electromagnetic loss [18,31,32]. Luo et al. [18] prepared bacterial-derived CNFs, which were used for the immobilization of Fe_3O_4 nanoparticles, and the minimum reflection loss (RL_{min}) reached −62.1 dB at 9.12 GHz. Zhou et al. [31] fabricated porous Fe_3O_4/CNFs and investigated the effect of the calcination temperature on the microstructure and dielectric properties. Finally, an RL_{min} of −42.25 dB with an effective absorption bandwidth (EAB) of 6.72 GHz was obtained.

The freeze-drying method is often used to produce cellulose aerogels as the precursors for CNFs. However, there is strong hydrogen bonding between cellulose molecules, resulting in the agglomeration of cellulose nanofibers. So, cellulose at a low concentration (below 1 wt%) is required to obtain highly porous cellulose aerogels, which reduces the production efficiency. In this work, cellulose aerogels were produced by freeze-drying oil in water (O/W) emulsions with cyclohexene (CHE) as the oil phase and 1 wt% cellulose nanofibers as the water phase (Figure 1). The microstructures and composition of the CNFs were characterized and the MA performances were investigated. In addition, the impact of the CHE volume ratio on the microstructure and MA performance of the CNFs were also analyzed and discussed in detail. Finally, the corresponding MA mechanism was also explained in this work.

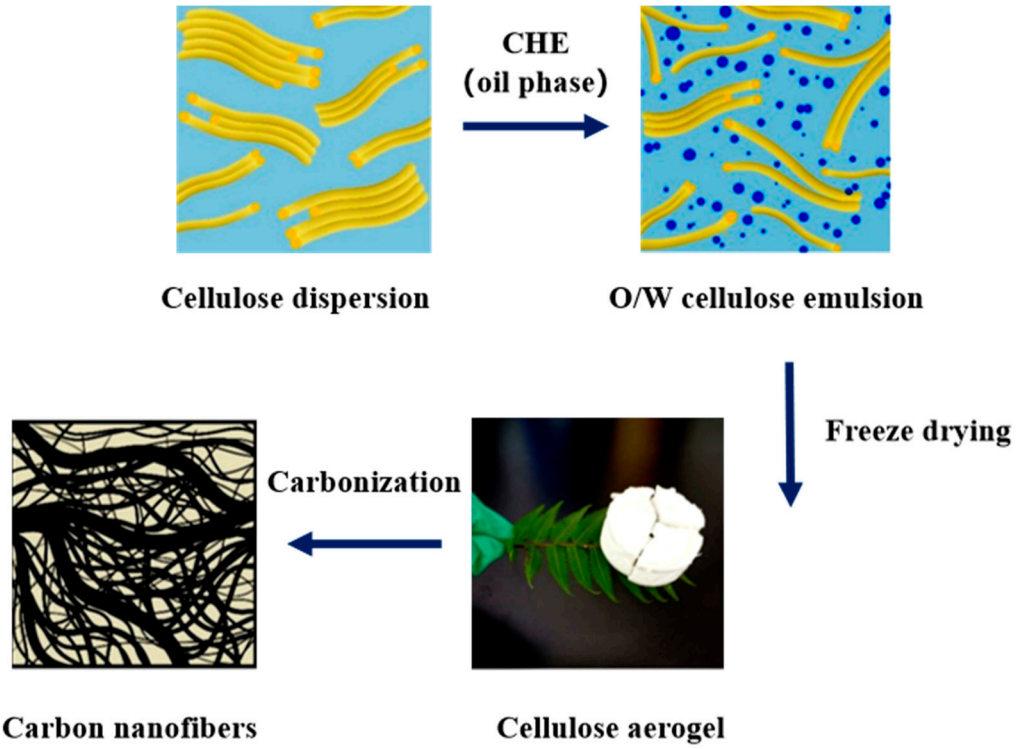

Figure 1. The schematic illustration of the preparation process of the CNFs using freeze-drying and carbonization.

2. Results and Discussion

2.1. Morphology and Microstructure of Cellulose Aerogels and CNFs

Liquid emulsions are often prepared by suspending the oil phase in the aqueous phase by emulsification [33]. As shown in Figure 1, the cellulose nanofiber dispersion was used as the water phase, and the CHE was added as the oil phase to prepare the O/W emulsions. During this process, the CHE was converted into micro-sized droplets by ultrasonic emulsification to weaken the hydrogen bonds between the cellulose nanofibers. The morphologies of the cellulose aerogels and CNFs were characterized by field emission scanning electron microscopy (FESEM). As shown in Figure 2a, it was found that the microstructure of the pure cellulose aerogel was a lamellar structure formed by the cellulose nanofibers. It has been reported that cellulose nanofibers are easily reunited and aggregated into a lamellar structure due to the hydrogen bonding between the large amounts of hydroxyl groups on the cellulose surface [34]. However, from Figure 2b, the cellulose nanofiber aerogel after adding of 25 vol % CHE gave a more dispersed network structure. This indicated that the agglomeration of the cellulose nanofibers due to freeze-drying was effectively reduced by the micro-sized droplets of the CHE in the O/W cellulose emulsion. The CHE was emulsified into micro-sized droplets and evenly mixed with cellulose dispersion in the emulsion [35]. The micro-sized droplets of the CHE in the cellulose dispersion effectively improved the dispersion of the cellulose nanofibers by destroying the hydrogen bonding interactions. After the freeze-drying, the CHE and water were sublimated and cellulose aerogels with 3D network frameworks were obtained. In addition, it was observed that the structure of the cellulose aerogels was well preserved during the subsequent carbonization (Figure 2c) and the diameter of the produced CNFs was above 20 nm. These results prove that the dispersion effect of CHE was effective for constructing highly porous CNFs with 3D network structures.

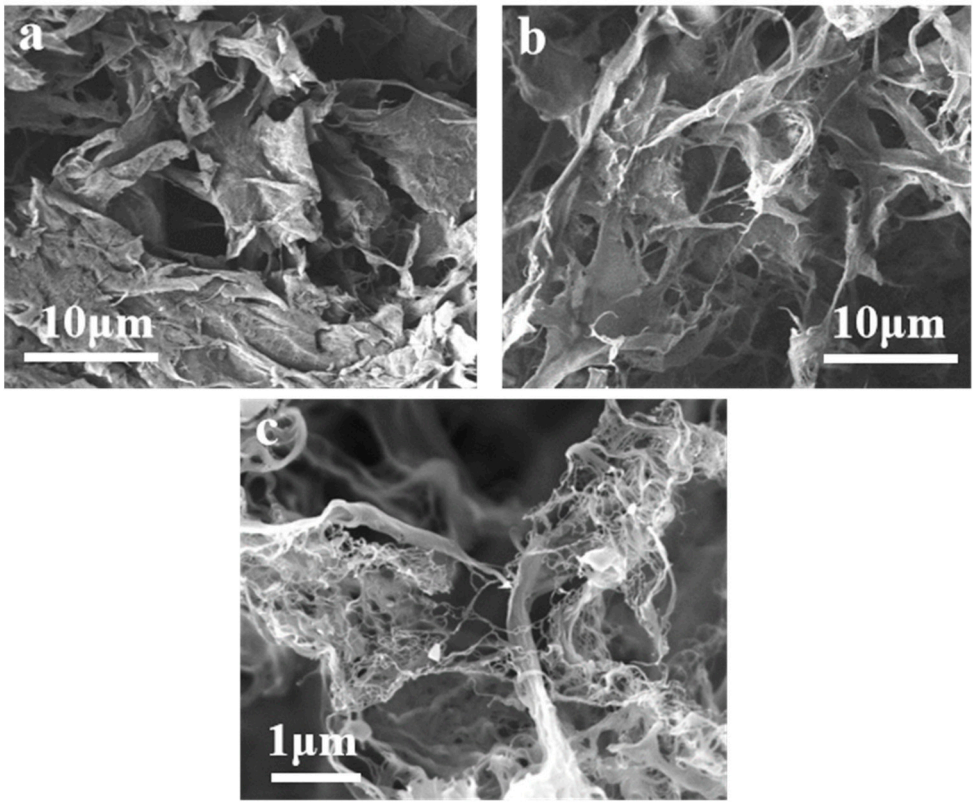

Figure 2. FESEM images: (**a**) cellulose aerogel produced from 1 wt% cellulose nanofiber dispersion; (**b**) cellulose aerogel from the emulsion containing 25 vol% CHE; (**c**) CNF-25.

2.2. Chemical Compositions of CNFs

Figure 3a shows the X-ray diffraction (XRD) pattern of the CNF-25. From the XRD pattern, it was found that the peak around 2θ = 25.5°corresponded to the (002) diffraction plane of hexagonal graphite in the standard card (JCPDS 26-1077). The insert of Figure 3a corresponds to the XRD pattern of the cellulose aerogel, and a sharp peak at 2θ = 22.0° attributed to the cellulose-I crystal structure was observed, which was obviously different from that of CNF-25 [27]. The valence states and chemical compositions of CNF-25 were analyzed by X-ray photoelectron spectroscopy (XPS). Figure 3b confirms the presence of C and O elements with no other impurities, and the ratio of the O/C content was 0.094. As shown in Figure 3c, the C1s peak was split into two components at ~284.6 eV and ~288.1 eV, corresponding to the sp^2C=C bond in the aromatic group and C=O bond, respectively [34,36]. The relative proportion of the sp^2C=C bonds in the aromatic group was 56.01%, and there were some residual oxygen-containing groups in the CNFs. Figure 3d gives the Raman spectra of the CNFs obtained from different proportions of CHE. Two peaks for the D bond (ca. 1330 cm^{-1}) and G bond (ca. 1590 cm^{-1}) appeared in the Raman spectra [37,38]. Meanwhile, I_D/I_G refers to the intensity ratio between the D and G bond and indicates the degree of graphitization of the carbon material [39]. As shown in Figure 3e, the I_D/I_G ratio of CNF-0, CNF-5, and CNF-25 were 0.79, 0.85, and 0.90, respectively. It was obvious that the I_D/I_G ratio was visibly increased with the proportion of the CHE. It was also concluded that the greater CHE volume resulted in more lattice defects in the CNFs, and these defects probably provided the polarization center to facilitate the absorption of electromagnetic waves [31,40,41].

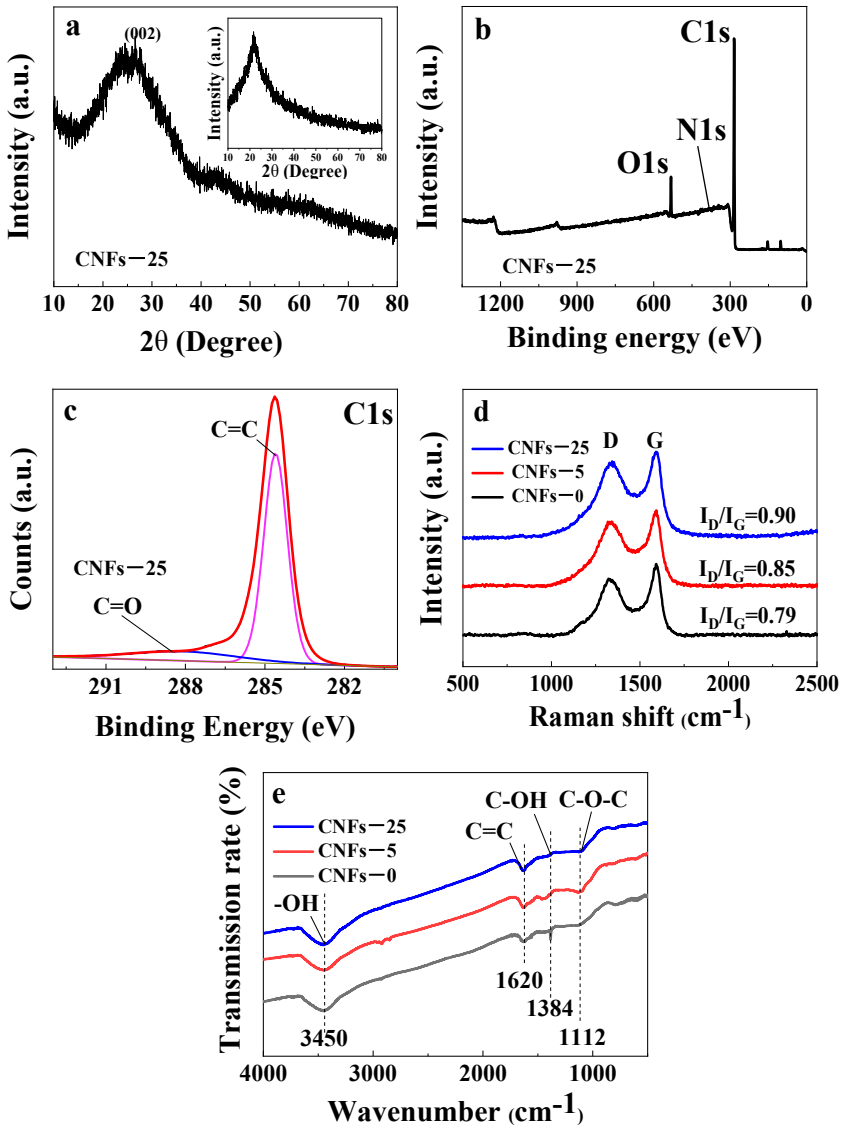

Figure 3. Composition analysis results: (**a**) XRD patterns; (**b**) XPS survey spectra; (**c**) C1s XPS spectrum; (**d**) Raman spectra; and (**e**) FTIR spectra from the produced CNFs.

Figure 3e shows the Fourier transform infrared spectroscopy (FTIR) spectra of CNF-0, CNF-5, and CNF-25. The broad bond with the range from 3500 to 3330 cm^{-1} was attributed to the O-H stretching vibration of the hydroxyl groups of the absorbed water molecules and hydroxyl groups on the surface of the CNFs. The band at 1620 cm^{-1} was assigned to the C=C stretching vibration. The band at 1384 cm^{-1} corresponded to the C-OH skeletal stretching vibration, and the band at 1112 cm^{-1} was from the C-O-C glycoside links derived from the cellulose molecular chains [26,27].

2.3. Dielectric Properties of CNFs

The frequency dependence of the real permittivity (ε') and imaginary permittivity (ε'') of the CNFs is shown in Figure 4. The relationship between the permittivity and the frequency can be interpreted by the Debye relaxation theory, as expressed in Equations (1) and (2) [42].

$$\varepsilon' = \varepsilon_\infty + \frac{\varepsilon_s - \varepsilon_\infty}{1 + \omega^2\tau^2} \quad (1)$$

$$\varepsilon'' = \frac{\varepsilon_s - \varepsilon_\infty}{1 + \omega^2\tau^2}\omega\tau + \frac{\sigma}{\omega\varepsilon_0} \quad (2)$$

where ε_s is the static permittivity and ε_∞ is the relative dielectric permittivity at the high-frequency limit, ω is the angular frequency, τ is the polarization relaxation time, σ is the electrical conductivity, and ε_0 is the dielectric constant in vacuum (8.854×10^{-12} F/m).

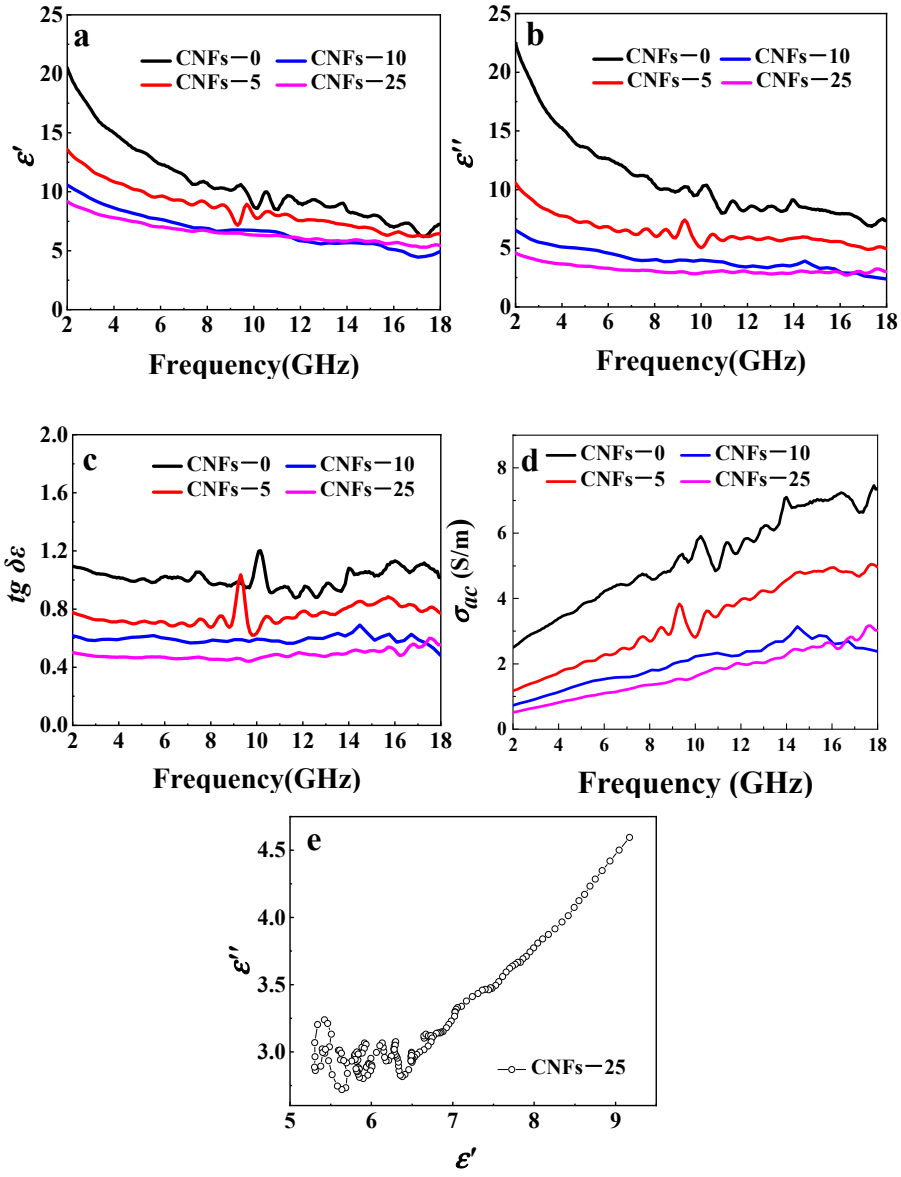

Figure 4. Electromagnetic parameters: (**a**) the real dielectric value; (**b**) imaginary value; (**c**) loss tangent; (**d**) AC conductivity; and (**e**) the Cole–Cole curve of CNFs.

According to Equations (1) and (2), ε' is associated with the variable of polarization under the action of an external electric field, which represents the storage capability of electric energy [41]. ε'' represents the loss capability of the electric energy associated with the enhanced polarization loss and the leakage loss [43]. The dielectric loss tangent ($tan\delta = \varepsilon''/\varepsilon'$) corresponds to the dielectric loss capacity, and a larger $tan\delta$ indicates a stronger loss capacity of the electromagnetic wave [4]. Overall, ε' and ε'' typically decrease with the increasing frequency, which is explained by the free electron theory or Debye equations [5,31]. Under the action of electromagnetic waves, polarization occurred due to the presence of the conductive CNFs. ε', ε'', and $tan\delta$ showed a significant downward trend with the increase in the CHE volume ratio because more structural defects were negative for the formation of complete conductive networks (Figure 4a–c). Figure 4d corresponds to the AC conductivity of the CNFs with different CHE volumes. It was observed

that the AC conductivity decreased with the increase in the CHE volume. This also indicated that although the CHE improved the amount of lattice defects, the electron transfer was suppressed.

To further investigate the dielectric loss mechanism of the CNFs, the curves of ε'–ε'' were plotted (Figure 4e). A Debye relaxation process generally induces a semicircle, as formulated by the Cole–Cole Equation (3) deduced from Equations (1) and (2) [42]. A semicircle in the Cole–Cole plot represents one Debye relaxation process.

$$\left(\varepsilon' - \frac{\varepsilon_s + \varepsilon_\infty}{2}\right)^2 + (\varepsilon'')^2 = \left(\frac{\varepsilon_s - \varepsilon_\infty}{2}\right) \quad (3)$$

It is well known that four types of polarization exist in a heterogeneous system: electronic, atomic, Debye (dipolar), and interfacial polarization. In this work, only Debye and interfacial polarization were considered because the electronic and atomic polarization usually occurred at higher frequencies. As shown in Figure 4e, for the CNFs, there were at least four semicircles over 2–18 GHz, in which a semicircle of the Cole–Cole plot represents one Debye relaxation process [31]. This suggested that there was a multi-relaxation process inside the material, which was the main cause of the dielectric loss. Under the action of electromagnetic waves, the polarization center, electron polarization, and interface polarization were generated, resulting in the loss of the electromagnetic wave. Besides the semicircles, the straight line at the end of the curve also indicated that the conductive loss contributed to the electromagnetic absorption. Thus, the MA performance of the resulting CNFs was attributed to the multiple polarization loss and the conductive loss.

2.4. Electromagnetic Absorption Performance and Mechanism of CNFs

The reflection loss (*RL*) value, matching thickness (t_m), and effective absorption bandwidth (EAB, frequency range with $RL < -10$ dB) are important standards for evaluating the electromagnetic wave absorption performance of absorbers. Figure 5 shows the *RL* values of the CNFs with different emulsion components at 2–18 GHz. From Figure 5a–c, it was found that the CNF-25 exhibited a greater MA performance with an increase in the proportion of CHE at the same filling ratio (2 wt%). The CNF-25 with 2 wt% filler loading exhibited an RL_{min} of −42.18 dB with an EAB of 4.9 GHz ranging from 8.9 GHz to 13.8 GHz. In addition, the values of *RL* gradually moved to the low frequency with the increase in thickness, which was consistent with the theory of 1/4 wavelength [44].

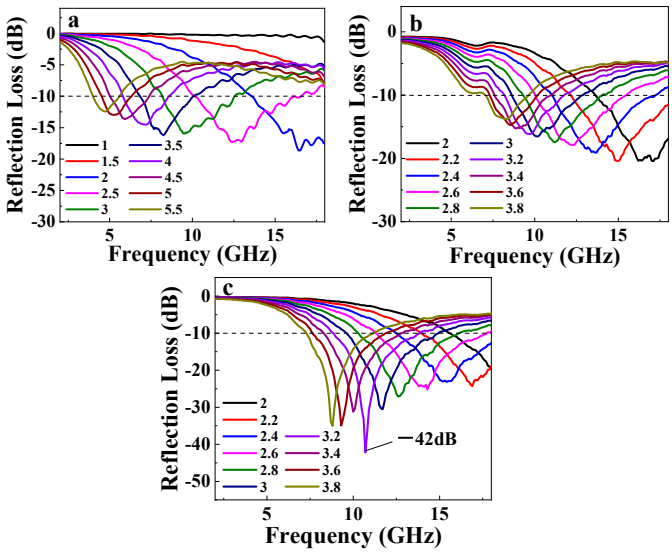

Figure 5. *RL* curves over 2–18 GHz at different thicknesses of 2–3.8 mm: (**a**) CNF-0; (**b**) CNF-5; and (**c**) CNF-25. The CNF loading amount was 2 wt %.

There are two basal principles for designing absorber materials: the impedance matching and the electromagnetic attenuation capacity [1]. According to the electromagnetic theory, the higher volume percentage of air can optimize the impedance matching [2,4]. Thus, porous CNFs with good conductive networks benefit the impedance matching of absorbers. In addition, there were residual oxygen-containing functional groups and carbon lattice defects in the CNFs, which also enhanced the electromagnetic wave penetration and absorption by improving the impedance matching and polarization from the defects and dipoles [31]. Figure 6a shows the impedance matching $|Z_{in}/Z_0|$ value from the CNFs produced from different CHE volumes, which was calculated using Equations (4) and (5).

$$Z_0 = \left(\frac{\mu_0}{\varepsilon_0}\right)^{\frac{1}{2}} \tag{4}$$

$$Z_{in} = Z_0\left(\sqrt{\frac{\mu_r}{\varepsilon_r}}\right) tanh\left[j\left(\frac{2\Pi fd}{c}\right)\left(\sqrt{\mu_r\varepsilon_r}\right)\right] \tag{5}$$

where Z_0 is the free space impedance and Z_{in} is the input impedance, d stands for the coating thickness, and μ and ε correspond to the complex permeability and permittivity, respectively. When the $|Z_{in}/Z_0|$ value is 1, this indicates that the incident electromagnetic waves can completely enter the material to ensure the maximum absorption of the electromagnetic waves. It was found that CNF-25 gave good impedance matching (from 0.8 to 1.2) compared with CNF-5 and CNF-0, which is possibly attributed to the 3D conductive network and many defects in the CNFs produced from high CNE volumes. After that, the MA capability is mostly dependent on the attenuation constant α calculated using electromagnetic parameters, which is expressed as Equation (6) [45]:

$$\alpha = \frac{\sqrt{2}\pi f}{c}\sqrt{(\mu''\varepsilon'' - \mu'\varepsilon') + \sqrt{\left((\mu''\varepsilon'' - \mu'\varepsilon')^2 + (\mu'\varepsilon'' - \mu''\varepsilon')^2\right)}} \tag{6}$$

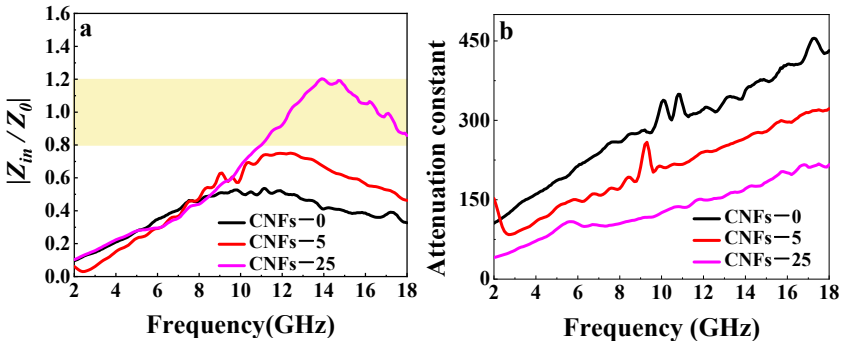

Figure 6. Basal principles for designing absorber material: (**a**) characteristic impedance and (**b**) attenuation constants α of CNFs.

The attenuation constant α of the CNFs was collected and is plotted in Figure 6b. It was found that CNF-0 exhibited the highest α value among these CNF materials. It was consistent with the high ε' and ε'' of CNF-0 due to its strong polarization and loss properties. For CNF-25, the attenuation constant was low compared with that of CNF-0 and CNF-5. However, CNF-25 exhibited great MA performance, as seen in Figure 5. So, even if CNF-0 showed a high attenuation constant, the electromagnetic wave was still reflected on the surface and could not enter into the material inside owing to the impedance mismatching. These results indicated that both the strong attenuation constant α and proper characteristic impedance achieved the optimum MA performance for the CNFs. Compared with the reported carbon-based MA materials, the resulting CNFs still exhibited a good MA capacity with the very low loading of 2 wt% (Table 1) [6,46–50].

Table 1. Comparison of the reported carbon-based absorbers with the produced CNFs.

Materials	Fill Loadings	RL_{min} (dB)	EAB (GHz)	Thickness (mm)	Ref.
CNFs	2 wt%	−42.18	4.90	2.00	This work
CB/RGO	7 wt%	−47.50	5.92	2.20	[6]
HCDC-30	8 wt%	−47.00	5.50	1.90	[46]
AC/Epoxy	40 wt%	−39.57	2.14	3.0	[47]
PAN-based CNFs	10 wt%	−12.75	4.88	2.2	[48]
B,N-CNTs	10 wt%	−40.00	4.9	2.0	[49]
RGO/PVDF	3 wt%	−25.6	4.3	4.0	[50]

According to the microstructure and MA capacity of the CNFs, the results indicated that the electromagnetic absorption was mainly related with the polarization and conduction loss. With the CHE as the oil phase, highly porous CNFs with good conductive networks were obtained. Large amounts of carbon lattice defects and oxygen-containing groups appeared, which acted as the polarization center for microwave attenuation. In addition, the CNFs exhibited 3D conductive networks, which increased the electron transfer and enhanced the conductive loss. So, the produced CNFs with lots of defect sites, oxygen-containing groups, and good conductivity showed the optimization of impedance matching and an excellent MA performance.

3. Experimental Procedures

3.1. Chemicals and Reagents

The 4 wt% cellulose nanofiber gel was obtained from Jinan Sheng Quan group Co., Ltd. (Jinan, China).

The gel was extracted from straw crops. Distilled water was used to prepare the cellulose dispersions. CHE (purity 99%, AR) was purchased from Sinopharma Chemical Reagent Co., Ltd. (Shanghai, China).

3.2. Preparation of Cellulose Aerogels and CNFs Using Freeze-Drying Method

Cellulose aerogels were prepared using a simple freeze-drying method. In a typical preparation process, 4 wt% cellulose gel was evenly diluted into 1 wt% cellulose dispersion by ultrasonic dispersion. While stirring at 700 rpm, the CHE was slowly added to 20 mL of cellulose dispersions with different concentrations followed by ultrasonic emulsifying at 150 W (FS-250, China) for 1 min to obtain the O/W emulsions. The cellulose emulsions were immersed into liquid nitrogen for 5–8 min, and freeze-dried at −60 °C for 48 h with a freeze-drier (SCIENTZ-10 N, Ningbo, China). Finally, the lightweight cellulose aerogels were obtained.

The prepared cellulose aerogels were carbonized in a tube furnace at 800 °C for 2 h under N_2 atmosphere at a heating rate of 5 °C min^{-1} and cooled to room temperature. To further investigate the role of CHE, other CNFs were also prepared from the emulsions with different CHE volumes as the oil phase. The resulting CNFs were labeled as CNF-x (where x referred to the volume percent of CHE in the emulsions), which was CNF-0, CNF-5, CNF-10, and CNF-25, respectively.

3.3. Characterization

The morphology of cellulose aerogels and CNFs were observed by FESEM (JSM-7610F, Tokyo, Japan) at 15 kV. XRD measurement was carried out using a Miniflex 600 X-ray diffractometer (Tokyo, Japan) with Cu Kα radiation (λ = 1.5418 Å, 40 kV, 40 mA) in the range of 2θ = 10–80°. The chemical bonds of CNFs were investigated by an FTIR spectrometer (FTIR 850, Tianjin, China). Raman spectra were recorded on a Raman spectroscope (Raman, in Via, England) with 532 nm laser. XPS was performed using a Thermo Fisher K-Alpha instrument (Waltham, MA, USA) and the data were analyzed by Casa XPS software 2.3.

3.4. Electromagnetic Absorption Measurement

In order to measure the electromagnetic absorption of the CNFs, the CNFs were evenly mixed with paraffin with a mass ratio of 2 wt%. Then, the mixtures were compressed into cylindrical-shaped specimens under 2 MPa for 2 min (Φ_{out} = 6.99 ± 0.07% mm, Φ_{in} = 3.04 ± 0.03% mm and thickness =2.71 ± 0.02% mm). The electromagnetic parameters of CNFs were measured with air coaxial line method in the frequency range of 2–18 GHz with Agilent N1500A vector network analyzer. Based on the transmission line theory, the reflection loss is up to the measured electromagnetic parameters according to the following equations [51]:

$$RL = 20log(|Z_{in} - Z_0|/|Z_{in} + Z_0|) \quad (7)$$

where the input impedance (Z) can be described as

$$Z_{in} = \sqrt{\frac{\mu_r}{\varepsilon_r}} tanh\left(\frac{j2\pi fd}{c\sqrt{\mu_r\varepsilon_r}}\right) \quad (8)$$

where ε_r ($\varepsilon_r = \varepsilon' - j\varepsilon''$) and μ_r ($\mu_r = \mu' - j\mu''$) refer to the complex permittivity and permeability of the material, respectively, f is the microwave frequency, d represents the thickness of the absorber, and c is the light velocity.

4. Conclusions

In summary, highly porous CNFs with 3D conductive networks have been successfully produced by freeze-drying the O/W emulsions and using the carbonization method. It was found that the addition of CHE as the oil phase could effectively weaken the hydrogen bonding in the cellulose and prevent its agglomeration during the freeze-drying. The electromagnetic parameters, including the dielectric constant and AC conductivity, were easily adjusted by changing the CHE volume. These results indicated that CNF-25 exhibited the best MA performance, in which the RL_{min} was up to −42.18 dB with a wide EAB of 5 GHz at 2 mm and a filling ratio of 2 wt%. The high MA performance was attributed to the fact that the high CHE volume effectively increased the amounts of lattice defects and residual oxygen-containing groups as the polarization centers, which was positive for the optimization of impedance matching. In addition, the good conductive networks in the CNFs also enhanced the conductive loss. This work has developed a new route for producing cellulose-derived CNFs from freeze-drying emulsions, which exhibits potential and promising applications for lightweight high-performance carbon-based MA materials.

Author Contributions: Conceptualization, A.L.; methodology, A.L. and L.Q.; data curation, A.L.; writing—original draft preparation, Z.L. and L.Q.; writing—review and editing, L.Q.; supervision. All authors have read and agreed to the published version of the manuscript.

Funding: This work is supported by the Foundation (No. KF202111) of Key Laboratory of Pulp and Paper Science & Technology of Ministry of Education, Qilu University of Technology (Shandong Academy of Sciences).

Data Availability Statement: Data are contained within the article.

Conflicts of Interest: The authors declare no conflict of interest.

References

1. Green, M.; Chen, X. Recent progress of nanomaterials for microwave absorption. *J. Mater.* **2019**, *5*, 503–541. [CrossRef]
2. Zhao, H.Q.; Cheng, Y.; Liu, W.; Yang, L.; Zhang, B.; Wang, L.P.; Ji, G.; Xu, Z.J. Biomass-derived porous carbon-based nanostructures for microwave absorption. *Nano-Micro Lett.* **2019**, *11*, 81–97. [CrossRef] [PubMed]
3. Ge, C.; Wang, L.; Liu, G. Research progress in carbon-based/carbonyl iron composite microwave absorption materials. *J. Mater. Eng.* **2019**, *47*, 43–54.
4. Wu, Z.; Tian, K.; Huang, T.; Hu, W.; Xie, F.; Wang, J.; Su, M.; Li, L. Hierarchically porous carbons derived from biomasses with excellent microwave absorption performance. *ACS Appl. Mater. Interfaces* **2018**, *10*, 11108–11115. [CrossRef] [PubMed]
5. Kuang, B.; Ning, M.; Wang, L.; Li, J.; Wang, C.; Hou, Z.; Zhao, Y.; Jin, H. Biopolymer nanofiber/reduced graphene oxide aerogels for tunable and broadband high-performance microwave absorption. *Compos. Part B* **2019**, *161*, 1–9. [CrossRef]

6. Tang, J.; Bi, S.; Wang, X.; Hou, G.-L.; Su, X.-J.; Liu, C.-H.; Lin, Y.-Y.; Li, H. Excellent microwave absorption of carbon black/reduced graphene oxide composite with low loading. *J. Mater. Sci.* **2019**, *54*, 13990–14001. [CrossRef]
7. Wu, M.; Qi, X.; Xie, R.; Bai, Z.; Qin, S.; Zhong, W.; Deng, C. Graphene oxide carbon nanotubes/ $Co_xFe_{3-x}O_4$ ternary nanocomposites: Controllable synthesis and their excellent microwave absorption capabilities. *J. Alloys Compd.* **2020**, *813*, 151996. [CrossRef]
8. Qin, F.; Brosseau, C. A review and analysis of microwave absorption in polymer composites filled with carbonaceous particles. *J. Appl. Phys.* **2012**, *111*, 061301. [CrossRef]
9. Cheng, J.; Zhao, H.; Li, M.; Li, S.; Wang, Y. Research progress on carbon-based microwave absorption materials. *Materials China* **2019**, *38*, 897–905.
10. Singh, V.; Shukla, A.; Patra, M.; Saini, L.; Jani, R.; Vadera, S.; Kumar, N. Microwave absorbing properties of a thermally reduced graphene oxide/nitrile butadiene rubber composite. *Carbon* **2012**, *50*, 2202–2208. [CrossRef]
11. Guan, Z.; Jiang, J.; Yan, S.; Sun, Y.; Zhen, L. Sandwich-like cobalt/reduced graphene oxide/cobalt composite structure presenting synergetic electromagnetic loss effect. *J. Colloid Inter. Sci.* **2020**, *561*, 687–695. [CrossRef] [PubMed]
12. Qin, F.; Brosseau, C. Comment on the electromagnetic property of chemically reduced graphene oxide and its application as microwave absorbing material. *Appl. Phys. Lett.* **2011**, *98*, 072906.
13. Kang, S.; Zhang, W.; Hu, Z.; Yu, J.; Wang, Y.; Zhu, J. Porous core-shell zeolitic imidazolate framework-derived Co/NPC@ZnO-decorated reduced graphene oxide for lightweight and broadband electromagnetic wave absorber. *J. Alloy Compd.* **2020**, *818*, 152932. [CrossRef]
14. Wang, Y.; Wang, H.; Ye, J.; Shi, L.; Feng, X. Magnetic CoFe alloy@C nanocomposites derived from ZnCo-MOF for electromagnetic wave absorption. *Chem. Eng. J.* **2020**, *383*, 123096. [CrossRef]
15. Zhang, X.; Wang, G.; Cao, W.; Wei, Y.; Liang, J.; Guo, L.; Cao, M. Enhanced microwave absorption property of reduced graphene oxide (RGO)-$MnFe_2O_4$ nanocomposites and polyvinylidene fluoride. *ACS Appl. Mater. Interfaces* **2014**, *6*, 7471–7478. [CrossRef]
16. Zhang, K.; Zhang, J.; Hou, Z.; Bi, S.; Zhao, Q. Multifunctional broadband microwave absorption of flexible graphene composites. *Carbon* **2019**, *141*, 608–617. [CrossRef]
17. Lou, Z.; Wang, Q.; Kara, U.; Mamtani, R.; Zhou, X.; Bian, H.; Yang, Z.; Li, Y.; Lv, H.; Adera, S. Biomass-derived carbon heterostructures enable environmentally adaptive wideband electromagnetic wave absorbers. *Nano-Micro Lett.* **2022**, *14*, 1–16. [CrossRef]
18. Luo, H.; Zhang, Y.; Yang, Z.; Xiong, G.; Wan, Y. Constructing superior carbon-nanofiber-based composite microwave absorbers by engineering dispersion and loading of Fe_3O_4 nanoparticles on three-dimensional carbon nanofibers derived from bacterial cellulose. *Mater. Chem. Phys.* **2017**, *201*, 130–138. [CrossRef]
19. Corma, A.; Iborra, S.; Velty, A. Chemical routes for the transformation of biomass into chemicals. *Chem. Rev.* **2007**, *107*, 2411–2502. [CrossRef]
20. Wang, Y.; Gao, X.; Zhou, H.; Wu, X.; Zhang, W.; Wang, Q.; Luo, C. Fabrication of biomass-derived carbon decorated with $NiFe_2O_4$ particles for broadband and strong microwave absorption. *Powder Technol.* **2019**, *345*, 370–378. [CrossRef]
21. Xu, Y.; Zhang, F.; Zhai, W.; Cheng, S.; Li, J.; Wang, Y. Unraveling of Advances in 3D-Printed Polymer-Based Bone Scaffolds. *Polymers* **2022**, *14*, 566. [CrossRef] [PubMed]
22. Wang, Y.; Xu, Y.; Zhai, W.; Zhang, Z.; Liu, Y.; Cheng, S.; Zhang, H. In-situ growth of robust superlubricated nano-skin on electrospun nanofibers for post-operative adhesion prevention. *Nat. Commun.* **2022**, *13*, 5056. [CrossRef] [PubMed]
23. Lai, F.; Miao, Y.; Zuo, L.; Lu, H.; Huang, Y.; Liu, T. Biomass-derived nitrogen-doped carbon nanofiber network: A facile template for decoration of ultrathin nickel-cobalt layered double hydroxide nanosheets as high-performance asymmetric supercapacitor electrode. *Small* **2016**, *12*, 3235–3244. [CrossRef] [PubMed]
24. Yang, W.; Zhao, Z.; Wu, K.; Huang, R.; Liu, T.; Jiang, H.; Chen, F.; Fu, Q. Ultrathin flexible reduced graphene oxide/cellulose nanofiber composite films with strongly anisotropic thermal conductivity and efficient electromagnetic interference shielding. *J. Mater. Chem. C* **2017**, *5*, 3748–3756. [CrossRef]
25. Siro, I.; Plackett, D. Microfibrillated cellulose and new nanocomposite materials: A review. *Cellulose* **2010**, *17*, 459–494. [CrossRef]
26. Dumanli, A.; Windle, A. Carbon fibres from cellulosic precursors: A review. *J. Mater. Sci.* **2012**, *47*, 4236–4250. [CrossRef]
27. Jazaeri, E.; Tsuzuki, T. Effect of pyrolysis conditions on the properties of carbonaceous nanofibers obtained from freeze-dried cellulose nanofibers. *Cellulose* **2013**, *20*, 707–716. [CrossRef]
28. Jazaeri, E.; Zhang, L.; Wang, X.; Tsuzuki, T. Fabrication of carbon nanofiber by pyrolysis of freeze-dried cellulose nanofiber. *Cellulose* **2011**, *18*, 1481–1485. [CrossRef]
29. Zhou, L.; Xu, Z. Ultralight, highly compressible, hydrophobic and anisotropic lamellar carbon aerogels from graphene/polyvinyl alcohol/cellulose nanofiber aerogel as oil removing absorbents. *J. Hazard. Mater.* **2020**, *388*, 121804. [CrossRef]
30. Chen, L.; Huang, Z.; Liang, H.; Guan, Q.; Yu, S. Bacterial-Cellulose-Derived Carbon Nanofiber@MnO_2 and Nitrogen-Doped Carbon Nanofiber Electrode Materials: An Asymmetric Supercapacitor with High Energy and Power Density. *Adv. Mater.* **2013**, *25*, 4746–4752. [CrossRef]
31. Zhou, W.; Jiang, C.; Duan, X.; Song, J.; Yuan, Y.; Chen, N. Fe_3O_4/carbonized cellulose micro-nano hybrid for high-performance microwave absorber. *Carbohyd. Polym.* **2020**, *245*, 116531. [CrossRef] [PubMed]
32. Nanni, F.; Travaglia, P.; Valentini, M. Effect of carbon nanofibres dispersion on the microwave absorbing properties of CNF/epoxy composites. *Compos. Sci. Technol.* **2009**, *69*, 485–490. [CrossRef]

33. Guo, Q.; Cui, B.; Yuan, C.; Guo, L.; Li, Z.; Chai, Q.; Wang, N.; Gänzle, M.; Zhao, M. Fabrication of dry S/O/W microcapsule and its probiotic protection against different stresses. *J. Sci. Food Agric.* **2024**, *104*, 2842–2850. [CrossRef] [PubMed]
34. Gao, K.; Shao, Z.; Li, J.; Wang, X.; Peng, X.; Wang, W.; Wang, F. Cellulose nanofiber-graphene all solid-state flexible supercapacitors. *J. Mater. Chem. A* **2013**, *1*, 63–67. [CrossRef]
35. Wang, F.; Zhang, Y.; Li, X.; Wang, B.; Feng, X.; Xu, H.; Mao, Z.; Sui, X. Cellulose nanocrystals-composited poly (methyl methacrylate) encapsulated n-eicosane via a Pickering emulsion-templating approach for energy storage. *Carbohyd. Polym.* **2020**, *234*, 115934. [CrossRef]
36. Hu, H.; Zhao, Z.; Wan, W.; Gogotsi, Y.; Qiu, J. Ultralight and highly compressible graphene aerogels. *Adv. Mater.* **2013**, *25*, 2219–2223. [CrossRef]
37. Song, N.; Jiao, D.; Cui, S.; Hou, X.; Ding, P.; Shi, L. Highly Anisotropic thermal conductivity of layer-by-layer assembled nanofibrillated cellulose/graphene nanosheets hybrid films for thermal management. *ACS Appl. Mater. Interfaces* **2017**, *9*, 2924–2932. [CrossRef]
38. Wang, B.; Li, X.; Luo, B.; Yang, J.; Wang, X.; Song, Q.; Chen, S.; Zhi, L. Pyrolyzed bacterial cellulose: A versatile support for lithium ion battery anode Materials. *Small* **2013**, *9*, 2399–2404. [CrossRef]
39. Nemanich, R.; Solin, S. First- and second-order Raman scattering from finite-size crystals of graphite. *Phys. Rev. B* **1979**, *20*, 392–401. [CrossRef]
40. Gong, C.; Meng, H.; Zhao, X.; Zhang, X.; Yu, L.; Zhang, J.; Zhang, Z. Unique static magnetic and dynamic electromagnetic behaviors in titanium nitride/carbon composites driven by defect engineering. *Sci. Rep.* **2016**, *6*, 18927. [CrossRef]
41. Bora, P.; Azeem, I.; Vinoy, K.; Ramamurthy, P.C.; Madras, G. Morphology controllable microwave absorption property of polyvinylbutyral (PVB)-MnO_2 nanocomposites. *Compos. Part B* **2018**, *132*, 188–196. [CrossRef]
42. Fang, P. Cole—Cole Diagram and the Distribution of Relaxation Times. *J. Chem. Phys.* **1965**, *4*, 3411–3413. [CrossRef]
43. Wu, Q.; Gao, H.; Zhang, Y.; Shui, W. Microwave absorption and mechanical properties of cross-scale SiC composites. *Compos. Part B* **2018**, *155*, 83–91. [CrossRef]
44. Liu, X.; Yu, Z.; Ishikawa, R.; Chen, L.; Yin, X.; Ikuhara, Y.; Riedel, R. Single-source-precursor synthesis and electromagnetic properties of novel RGO-SiCN ceramic nanocomposites. *J. Mater. Chem. C* **2017**, *5*, 7950–7960. [CrossRef]
45. Vinoy, K.; Jha, R. *Radar Absorbing Materials—From Theory to Design and Characterization*; Kluwer Academic Publishers: Boston, MA, USA, 1996.
46. Wang, S.; Li, Q.; Hu, K.; Wang, S.; Liu, Q.; Kong, X. A facile synthesis of bare biomass derived holey carbon absorbent for microwave absorption. *Appl. Surf. Sci.* **2021**, *544*, 148891. [CrossRef]
47. Negi, P.; Kumar, A. Biomass-derived activated carbon/epoxy composite as microwave absorbing material. *J. Electron. Mater.* **2022**, *51*, 2918–2925. [CrossRef]
48. Dong, S.; Li, J.; Zhang, S.; Li, N.; Li, B.; Zhang, Q.; Ge, L. Excellent microwave absorption of lightweight PAN-based carbon nanofibers prepared by electrospinning. *Colloid. Surf. A* **2022**, *651*, 129670. [CrossRef]
49. Sun, Q.; Zhang, X.; Liu, R.; Shen, S.; Wu, F.; Xie, A. Tuning the dielectric and microwaves absorption properties of N-doped carbon nanotubes by boron insertion. *Nanomaterials* **2021**, *11*, 1164. [CrossRef]
50. Zhang, X.; Wang, G.; Cao, W.; Wei, Y.; Cao, M.; Guo, L. Fabrication of multi-functional PVDF/RGO composites a simple thermal reduction process and their enhanced electromagnetic wave absorption and dielectric properties. *RSC Adv.* **2014**, *4*, 19594–19601. [CrossRef]
51. Inui, T.; Konishi, K. Fabrications of broad-band RF-absorber composed of planar hexagonal ferrites. *IEEE Trans. Magn.* **1999**, *35*, 3148–3150. [CrossRef]